

A point plasma model for linear plasma devices based on SOLPS-ITER equations: application to helium plasma

E Tonello¹, A Formenti¹, G Alberti¹, A Uccello², M Passoni^{1,2}

¹ Politecnico di Milano, Department of Energy, Milan, 20133, Italy

² Istituto per la Scienza e Tecnologia dei Plasmi, CNR, Milan, 20125, Italy

E-mail: elena.tonello@polimi.it

Abstract. Linear plasma devices represent an essential tool for nuclear fusion research, whereby understanding crucial aspects related to plasma-wall interactions or edge plasma behavior. Simplified models are of great importance to complement and integrate experimental and simulation results of complex systems such as plasmas in linear machines, because they are fast and simple to employ.

In this work, we present a global volume-averaged (0D) model for plasma investigation in linear machines. The 0D model equations are based on the space integration of the state of the art edge plasma model implemented in the SOLPS-ITER code.

Comparisons between helium plasmas described with 2D simulations performed with SOLPS-ITER and with the 0D model highlight that contributions often neglected in tokamak edge models, e.g. electron-neutral excitation, may be relevant when describing weakly ionized plasmas in linear devices.

The model is used to perform sensitivity studies with respect to several parameters and to analyse the time evolution of the system, leading to the identification of two relevant time scales governing the system.

Lastly, a comparison of 0D results with experimental data from the linear device GyM is performed, showing satisfactory agreement.

Our methods and results provide crucial interpretative keys in the investigation of the physics of edge plasmas.

Keywords: linear plasma device, helium plasma, SOLPS-ITER, global model

1. Introduction

The problem of modelling the edge plasma in magnetic fusion devices is a very challenging one [1]. The plasma in this region is highly turbulent and, in many relevant situations, the regime of collisionality among particles is somewhat intermediate between the fluid approximation [2] and the kinetic description used for the core plasma. In the last forty years, different approaches were developed to address this problem. In the attempt to broadly classify them, we distinguish among mean-field fluid models [3], turbulent fluid models [4, 5, 6], hybrid fluid-kinetic models [7] and full gyrokinetic models [8]. Despite the attempt to move towards a description based on first-principles, today the mean-field fluid approach is still the most used, both in the design phase and for the interpretation of experiments. Numerical codes that implement this method are SOLEDGE2D [9] and SOLPS, whose latest release, named SOLPS-ITER [10, 11], is widely considered the state of the art tool for edge plasma modelling. This code implements a coupled numerical strategy based on a 2D multi-fluid description for the electron, main ion and impurity populations [12, 13] and a 3D kinetic description for neutral particles. It is able to reproduce realistic tokamak geometries and many magnetic configurations and, since its early versions, it was used as the standard tool for ITER design [14]. According to its modelling strategy, kinetic effects along \vec{B} are accounted for through flux limiters [15], while the turbulent cross-field transport is modelled as a convective-diffusive process [16].

The possibility to simulate the problem in a self consistent way, albeit with some simplifying assumptions, comes at the price of a very high computational cost and, in many cases, not straightforward interpretation of its results. The need for simplified conceptual frameworks to guide the interpretation of simulations results is recognized [17] and with this aim many reduced models were developed, among which the 2 Point Model (2PM) [18] the most known in edge plasma physics. This approach provides analytical formulae to derive steady-state plasma parameters at the divertor targets, prescribing the controlling upstream conditions. 2PM analysis derived from SOLPS and SOLEDGE2D equations are found in [19, 20, 21].

Global modelling represents another simplified numerical method of describing plasmas. Such an approach is able to predict spatially averaged (global) plasma parameters such as densities or temperatures, by solving ordinary differential equations (ODEs) and without knowing a priori upstream quantities. Although widely used in the investigation of low temperature plasmas with a complex chemical kinetics [22], global models are only scarcely used in the context of fusion research [23, 24, 25]. However, the development of a model based on the volume average of multi-dimensional fluid equations could give a direct connection with the results of codes like SOLPS. Neglecting most of the spatial dependencies of the problem, this method would provide a simple and fast tool, able to reproduce the general trends of quantities of interest in the edge plasma, such as temperature and density. The simple structure of the description, which in steady-state

reduces to a balance of several sources and sink terms, should, in turn, provide a more immediate interpretation of the physics governing the problem.

A global approach can be particularly appealing in connection with a simplified geometry to study the boundary plasma. In the latest years, there was a growing interest in the theoretical and experimental investigation of edge relevant conditions in linear plasma devices (LPDs). LPDs are simple and cost effective tools able to reproduce conditions of partially ionized plasmas and particle fluxes, which characterize the scrape-off layer and the divertor region in tokamaks. The presence of neutral particles enables the investigation of all the aspects related to plasma-neutral interaction, while the simple cylindrical geometry and the uniform magnetic field simplify the plasma modelling with respect to the transport problem.

In this work we present a point model, i.e. zero dimensional and space independent, based on the volume average of fluid equations for a magnetized plasma. The equations are obtained from the space integration of SOLPS-ITER model for a linear plasma device [26] or, when possible, from simplifying assumptions. The proposed model is then used to investigate helium plasma in the linear device GyM [27] and the results are compared with original two-dimensional simulations of the same physical system, done with the standard code SOLPS-ITER. The weakly ionized plasmas generated in LPDs offer a particularly suited environment to apply a global approach and this is particularly true for the low density sheath-limited regime [1], which features the plasma in GyM. As concerns the choice of helium, this decision is supported by a number of reasons. Helium will be present in the fuel mixture of next generation fusion reactors and earlier it will constitute the main plasma species in the first phase of ITER operation [28]. Thus, the investigation of such a species finds ample space among the current interests of the fusion community. Many experimental and computational studies were carried out in recent years: experimental detachment studies were performed in different LPDs, using helium as a working gas [29, 30, 31, 32]; a detailed collisional-radiative model was implemented in a 1D fluid model for the study of a detached helium plasma in NAGDIS-II [33]; the effect of helium on plasma-facing materials, such as tungsten, were extensively studied in LPDs, showing a variety of different surface modifications [34, 35, 36, 37]. Moreover, helium removes the complexities related to molecular species and it constitutes a suitable case-study for a newly developed model, allowing to reduce greatly the number of unknowns. From the conceptual point of view, generalizing our 0D model to other plasmas should be straightforward.

The structure of the paper is the following: after describing the point model in section 2, in section 3, we present the set up of original SOLPS-ITER simulations, which focuses on a parametric variation of the external input power and neutral background pressure. Besides the comparison of the point model with SOLPS-ITER simulations, in

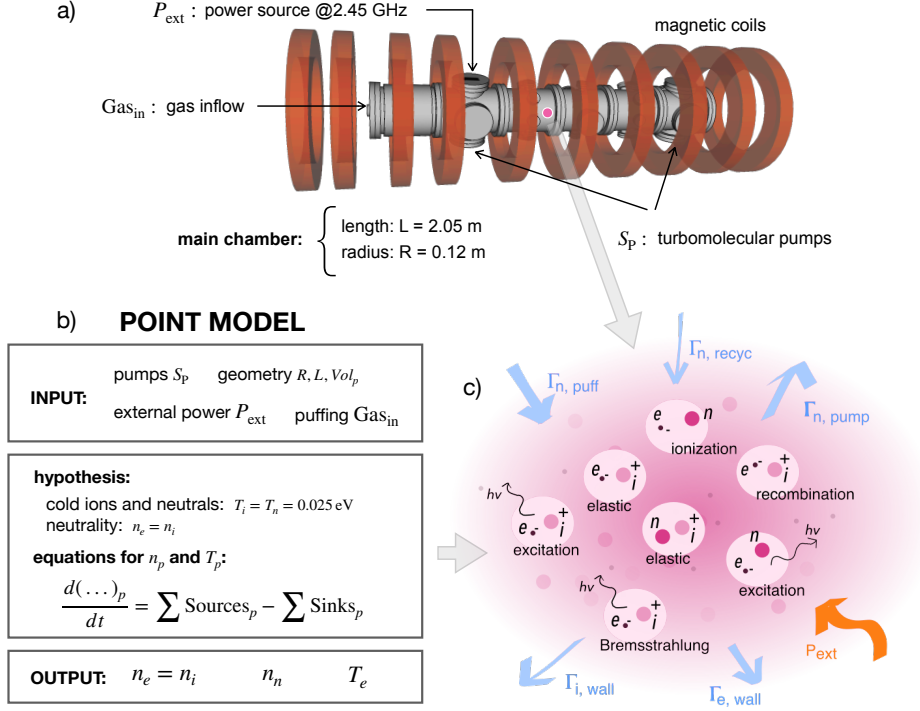


Figure 1. a) 3D CAD image of the linear plasma device GyM and its main components. b) Blocks containing the basic elements of the point model: the first block contains the model inputs; the second block synthetically describes the main hypotheses and the structure of the model equations; the third block specifies the outputs of the model. c) Visual representation of the point domain and the sources and sinks terms in the plasma balance equations: fluxes through the point domain boundaries, externally supplied power and atomic processes.

section 4, the point model is also used to extend the parametric study, derive analytical expressions for plasma and neutral densities, analyze the temporal evolution of the system and compare the results to experimental data from helium discharges in GyM.

2. Principles of the point plasma model for LPDs

A global point model to describe a plasma is based on a set of space independent balance equations describing density (n_p) and temperature (T_p) for each one of the considered populations (p). Such model has no interest in addressing the spatial variation of its variables, but rather it investigates in a simple and effective way the relative contributions of different source/sink mechanisms in determining a stationary plasma state.

As discussed in section 1, in this work, we are interested in investigating the weakly

ionized plasma in a linear device. LPDs are made of a cylindrical vacuum chamber surrounded by coils, which produce a magnetic field directed along the cylinder axis. Gas is injected inside the chamber through a puffing nozzle and pumped out by turbomolecular pumps, so that a stationary gas pressure is obtained. The plasma is generated by supplying external power to the neutral gas. Different source mechanisms are used in LPDs: arc discharge [38, 39, 40, 41], helicon waves [42, 43], electron cyclotron resonance (ECR) heating [26, 44]. Plasma is generated inside the chamber and flows along the magnetic field lines towards the basis of the cylinder, which we call targets. While streaming towards the targets, ions escape the magnetic confinement and undergo a slower radial cross-field motion.

To investigate this physical system, the model presented in this work assesses the time evolution of the average density and temperature for each population solving a system of ordinary differential equations in which the variation of the quantity of interest is expressed as a sum of source and sink contributions. In particular, we considered: atomic processes of ionization, recombination, electron excitation of neutral and ion ground states and elastic collisions; particle and heat losses due to plasma-wall interaction and particle recycling; active pumping and gas injection; heating by external source. A schematic summary of the basic elements of the model is shown in figure 1.b and 1.c.

As discussed, our model was developed to provide a simple tool for the interpretation of the results from SOLPS-ITER. For this reason, in developing its governing equations, we aimed at including most of the contributions that are present in the SOLPS-ITER physical model. Exceptions in this sense are the absence of plasma currents, since here global ambipolarity is assumed, as well as the absence of heat conduction contributions in the electron temperature balance, which is obtained from simplifying assumptions. Both these hypotheses, however, are well justified in the context of the sheath-limited plasma conditions expected in the GyM device.

Although the general ideas presented above can be extended to an arbitrary number of populations, the model presented here applies to a three populations plasma made of electrons (e), ions (i) and neutral atoms (n). The ionic population, moreover, only contains singly ionized atoms ($Z = 1$), consistently with the low ionization degree and temperature ($T_e \leq 15$ eV). Each population is represented by its values of density and temperature and our final goal is to solve a six-unknowns problem for n_e , T_e , n_i , T_i and n_n , T_n .

In the context of the modelling of typical LPDs, additional hypothesis can be made: first, plasma neutrality, as usually done in edge plasma models, is assumed and in our case simply reads $n_i = n_e$; second, neutral and ion temperatures are assumed to be constant and equal to room temperature, $T_i = T_n = 0.025$ eV. The hypothesis on T_n is usually well verified in the working regimes of LPDs, while, even if most of the external power is usually absorbed by electrons, ions can be heated up by collisions at sufficiently

high densities. The effect of a varying T_i is addressed separately in section 4.2.

Under these assumptions, the actual unknowns reduce to n_i , n_n and T_e and their evolution is described by the following equations:

$$\frac{dn_i}{dt} = R_{iz}n_en_n - R_{rc}n_en_i - \Gamma_{i,\text{wall}}n_i \quad (1)$$

$$\frac{dn_n}{dt} = -R_{iz}n_en_n + R_{rc}n_en_i + \Gamma_{n,\text{recyc}}n_i - \Gamma_{n,\text{pump}}n_n + \frac{\Gamma_{n,\text{puff}}}{\text{Vol}} \quad (2)$$

$$\begin{aligned} \frac{3}{2}n_e \frac{dT_e}{dt} = & \frac{P_{\text{ext}}}{\text{Vol}_e} - E_{iz}R_{iz}n_en_n - E_{i,\text{rad}}R_{i,\text{rad}}n_en_i \\ & - E_{n,\text{rad}}R_{n,\text{rad}}n_en_n - \Gamma_{e,\text{wall}}T_en_e \\ & - \frac{3}{2} \frac{2m_e}{m_i} R_{i,\text{el}}n_in_e(T_e - T_i) - \frac{3}{2} \frac{2m_e}{m_n} R_{n,\text{el}}n_n n_e(T_e - T_n) \\ & - \frac{3}{2} (R_{iz}n_en_n - R_{rc}n_en_i - \Gamma_{i,\text{wall}}n_i) T_e \end{aligned} \quad (3)$$

where, m_i and m_e are the ion and electron mass respectively and P_{ext} is the external power supplied to the electrons. A summary of the terms in the equations and their physical meaning are reported in table 1. A more detailed explanation is given in the following.

Volume reactions: A major contribution in the sources/sinks of our model is given by atomic reactions, which are characterized by reaction rate coefficients R .

The rate and power coefficients for ionization R_{iz} , recombination R_{rc} and excitation $E_{i,n,\text{rad}}R_{i,n,\text{rad}}$ are functions of the electron temperature and weakly depend also on the electron density. In this work, their values are taken from the ADAS/adf11 database (<https://open.adas.ac.uk>), which is the same database used in the SOLPS-ITER simulations. Bremsstrahlung was neglected for simplicity since its contribution was found negligible in the conditions under analysis.

The rate coefficient for elastic collisions among electrons and ions $R_{i,\text{el}} = \nu_{ei}/n_i$ is computed using the classical electron-ion collision frequency ν_{ei} from Coulomb collisions theory [45].

Lastly, the electron-neutral elastic rate coefficient is computed as $R_{n,\text{el}} = \sigma_{e,\text{el}}v_{e,\text{th}}$, where the cross section for electron-neutral elastic collisions $\sigma_{e,\text{el}}$ is taken from [46] and $v_{e,\text{th}}$ is the electron thermal velocity. The contribution of electron-neutral thermal equilibration is considered in our model, while it is disregarded in SOLPS-ITER.

Ion loss due to plasma-wall interaction: Besides volume reactions, we also consider boundary sources and sinks. The first one is $\Gamma_{i,\text{wall}}$, i.e. the ion loss contribution related to the sink action of the solid wall of the vacuum chamber. In this work, $\Gamma_{i,\text{wall}}$ is used to indicate the single particle contribution to the overall volume average flux at the boundary. Dimensionally, this quantity is the inverse of a time $\Gamma_{i,\text{wall}} = 1/\tau_{i,\text{wall}}$, where

Table 1. Summary of the different contributions to particles and energy balance equations in the global point model. Direct correspondence with the contributions shown in figure 1 should be seen.

Physical meaning	Formula/symbol	Units
Volume reactions		
Ionization	R_{iz}	$[\text{cm}^3 \text{s}^{-1}]$
Recombination	R_{rc}	$[\text{cm}^3 \text{s}^{-1}]$
Ionization energy loss	$E_{iz} R_{iz}$	$[\text{eV cm}^3 \text{s}^{-1}]$
Neutral excitation	$E_{n,\text{rad}} R_{n,\text{rad}}$	$[\text{eV cm}^3 \text{s}^{-1}]$
Ion excitation	$E_{i,\text{rad}} R_{i,\text{rad}}$	$[\text{eV cm}^3 \text{s}^{-1}]$
Electron-ion equilibration	$R_{i,\text{el}}(T_e - T_i) = \nu_{ei}/n_i(T_e - T_i)$	$[\text{eV cm}^3 \text{s}^{-1}]$
Electron-neutral equilibration	$R_{n,\text{el}}(T_e - T_n) = \sigma_{n,\text{el}}v_{e,\text{th}}(T_e - T_n)$	$[\text{eV cm}^3 \text{s}^{-1}]$
Contributions at the boundary		
Ion-to-wall sink	$\Gamma_{i,\text{wall}} = \Gamma_{i,\text{wall}\parallel} + \Gamma_{i,\text{wall}\perp}$	$[\text{s}^{-1}]$
Neutral recycling	$\Gamma_{n,\text{recyc}} = \beta\Gamma_{i,\text{wall}\parallel}$	$[\text{s}^{-1}]$
Neutral pumping ^a	$\Gamma_{n,\text{pump}} = S_P \times 1\text{e}3/\text{Vol}_n$	$[\text{s}^{-1}]$
Neutral puffing ^b	$\Gamma_{n,\text{puff}} = \text{Gas}_{\text{in}} \times 4.48\text{e}17$	$[\text{s}^{-1}]$
Electron-to-wall energy sink	$\Gamma_{e,\text{wall}} T_e$	$[\text{eV s}^{-1}]$

^a S_P is the total pumping speed, expressed in $[\text{l s}^{-1}]$

^b Gas_{in} is the mass inflow due to neutral gas puffing, expressed in Standard Cubic Centimeters per Minute [sccm]

$\tau_{i,\text{wall}}$ can be interpreted as the particle confinement time. In this context, thus, the quantity $\Gamma_{i,\text{wall}} n_i$ represents the number of particles lost due to the sink action of the wall, per unit time and per unit volume. This contribution is derived directly from the volume average of the corresponding term in the SOLPS-ITER[‡]:

$$\Gamma_{i,\text{wall}} n_i = \frac{1}{\text{Vol}_i} \int_{\text{Vol}_i} \left[\frac{1}{\sqrt{g}} \frac{\partial}{\partial x} \left(\frac{\sqrt{g}}{h_x} n_i^* v_{x,i}^* \right) + \frac{1}{\sqrt{g}} \frac{\partial}{\partial y} \left(\frac{\sqrt{g}}{h_y} n_i^* v_{y,i}^* \right) \right] \sqrt{g} dx dy dz \quad (4)$$

here h_x , h_y and h_z are the metric coefficients of the coordinate system and $\sqrt{g} = h_x h_y h_z$; Vol_i is the total volume occupied by the ions, which in principle can be different from the one occupied by neutrals Vol_n , due to the confining action of the magnetic field. In this work, since the plasma in GyM extends up to the lateral boundary of the cylinder, we considered $\text{Vol}_i = \text{Vol}_n$. The x , y and z reference frame for a LPD is shown in

[‡] Quantities indicated with \star represent space dependent variables, to distinguish them from global variables, which are the unknowns of the point model.

figure 2.a. According to SOLPS-ITER convention, x is along the axial magnetic field direction, while y and z are in the radial and azimuthal direction, respectively. On the RHS of equation (4), the first term represents transport parallel to the magnetic field $\Gamma_{i,\text{wall}\parallel} n_i$, while the second represents cross-field transport $\Gamma_{i,\text{wall}\perp} n_i$.

To obtain the volume averaged expressions of $\Gamma_{i,\text{wall}\parallel} n_i$ and $\Gamma_{i,\text{wall}\perp} n_i$, we applied Gauss theorem to equation (4) and we evaluated $n_i^* \mathbf{v}_i^* \cdot \mathbf{n}$ at the boundaries, where \mathbf{n} is the unit vector normal to the boundary surface. The parallel contribution $\Gamma_{i,\text{wall}\parallel} n_i$ is retrieved assuming the axial velocity at the targets equal to the Bohm velocity, $v_{x,i}^{*,T} = u_B \simeq \sqrt{T_e/m_i}$, under the assumption that $T_e \gg T_i$. Rigorously, this is valid at the electrostatic sheath entrance [1], but for the purposes of this work we will consider that sheath entrance and the actual wall surface to coincide. Moreover electron temperature is considered constant everywhere, $T_e^* = T_e$. For the contribution at the lateral boundaries, instead, we used the diffusion approximation for radial transport $v_{y,i} n_i^* = -D_\perp \partial n_i^* / (h_y \partial y)$, where D_\perp is the coefficient for anomalous diffusion, and the density decay length boundary condition $\lambda_n = -(\partial n_i^{*,Lat} / (n_i^{*,Lat} h_y \partial y))^{-1}$. The ratio D_\perp / λ_n has the dimensions of a velocity and can be regarded as the effective radial velocity at the boundary. With these assumptions, the integration of equation (4) gives:

$$\begin{aligned} \Gamma_{i,\text{wall}} &= \Gamma_{i,\text{wall}\parallel} + \Gamma_{i,\text{wall}\perp} \\ &= \frac{\alpha v_{x,i}^{*,T} A_T}{\text{Vol}_i} + \frac{v_{y,i}^{*,Lat} A_{Lat}}{\text{Vol}_i} = \frac{\alpha u_B A_T}{\text{Vol}_i} + \frac{D_\perp A_{Lat}}{\lambda_n \text{Vol}_i} \end{aligned} \quad (5)$$

where A_T and A_{Lat} are the target and lateral wall areas, respectively.

The effective coefficient for parallel transport $\alpha = n_{i,T}^* / n_i$ is defined as the ratio of the target plasma density over the point plasma density. Analytical expression for α can be found integrating a simple 1D ion momentum equation [1] along the distance covered by ions $L_{i,\text{tr}}$:

$$\frac{d}{dx} (m_i n_i^* v_{x,i}^{*2} + n_e^* T_e^*) = S_m \quad (6)$$

where we neglected ion pressure $p_i^* = n_i^* T_i^*$, under the assumption that $T_e \gg T_i$. We considered momentum loss due to ion-neutral friction, i.e. $S_m = -m_i R_{in,\text{el}} n_n^* n_i^* (v_{x,i}^* - v_{x,n}^*)$. Integrating equation (6), from the center of the device, $x = 0$, to the target, $x = L/2 = L_{i,\text{tr}}$, we assumed $v_{x,i}^*(0) = 0$ due to symmetry and, as a first approximation, we consider S_m to be constant, with $n_n^* = n_n$, $n_i^* = \alpha n_i$, $v_{x,i}^* = u_B$ and $v_{x,n} = 0$. We obtained:

$$\alpha = \frac{1}{2} \times \left[1 + \frac{m_i n_n L_{i,\text{tr}}}{2T_e} R_{in,\text{el}} u_B \right]^{-1} \quad (7)$$

where $\nu_{in,\text{el}} = R_{in,\text{el}} n_n$ is the ion-neutral collision frequency. The rate coefficient for ion-neutral elastic collisions is computed as $R_{in,\text{el}} = \sigma_{in,\text{el}} v_{i,\text{th}}$, where $v_{i,\text{th}}$ is the ion thermal velocity and the elastic collision cross section $\sigma_{in,\text{el}} = 1 \times 10^{-14} \text{ cm}^2$ at $T_i = 0.025 \text{ eV}$ is taken from the AMJUEL database (<http://www.eirene.de>). Comparing the value of

$S_m L_{i,\text{tr}}$, computed with constant S_m with the result of the actual integration of $\int S_m^* dx$, with S_m^* computed using space dependent n_n^* , n_i^* and $v_{x,i}^*$ from SOLPS-ITER simulations, we obtained a discrepancy up to factor of 3.

Neglecting ion-neutral friction, i.e. $S_m = 0$, equation (7) reduces simply to $\alpha = 1/2$.

Neutral recycling: Ions removed from the system due to plasma wall interaction (PWI) can either be trapped in the solid or be recycled as neutral atoms, after recombining with electrons of the solid.

In the global point model, the source of neutral particles coming back into the plasma after recycling is $\Gamma_{n,\text{recyc}} = \beta \Gamma_{i,\text{wall}\parallel}$, where $0 < \beta \leq 1$ is the recycling coefficient.

In SOLPS-ITER, the values of the recycling coefficient are usually computed from pre-compiled tables, obtained with the Monte Carlo code TRIM [47].

To account for surface saturation process in the plasma-facing materials (PFM), time dependent $\beta(t)$ which increases with time (or with ion fluence) up to unity, could be introduced in the model [48]. In the simulations presented here, the walls are considered to be saturated with helium and the effective coefficient for neutral recycling was set to the constant value $\beta = 1$ in all cases.

Electron energy loss due to plasma-wall interaction: Differently from particle contribution, electron energy losses at the plasma sheath are not obtained from a rigorous integration of SOLPS-ITER equation. In sheath-limited condition, typical of the low-density plasmas we are considering, this contribution can conveniently be computed following the basic treatment to obtain the sheath transmission coefficient [1], considering again a constant value for $T_e^* = T_e$.

Neglecting secondary electron emission and considering floating targets, the energy lost by the electron population at the sheath entrance per unit time and volume is:

$$\Gamma_{e,\text{wall}} T_e n_e = (2 + |eV_s| + |eV_{ps}|) T_e \Gamma_{i,\text{wall}\parallel} n_i \quad (8)$$

where we have assumed parallel ambipolarity, $j_x = 0$. The first contribution to equation (8) is due to the one-way Maxwellian heat flux of electron distribution onto the wall; the second one is the energy loss due to the sheath potential drop, $|eV_s| = 0.5 \ln[(2\pi m_e/m_i)(1 + T_i/T_e)]$ is expressed in unit of T_e ; lastly, the third one is the pre-sheath potential drop contribution, where the pre-sheath potential drop is computed from Boltzmann relation, $|eV_{ps}| = \ln \alpha$, again in unit of T_e . In this model only parallel electron energy loss is considered, neglecting radial energy losses.

A more sophisticated 0D electron energy equation, based on a rigorous integration of the full fluid equation, can become necessary when one is interested in investigating higher densities regimes. In these conditions, parallel temperature gradients are no longer negligible and conduction heat losses should be taken into account. At high density, also ion energy balance can play a role due to the higher collisionality. Following the procedure used above for particle balance, a generalization of the electron and, if needed,

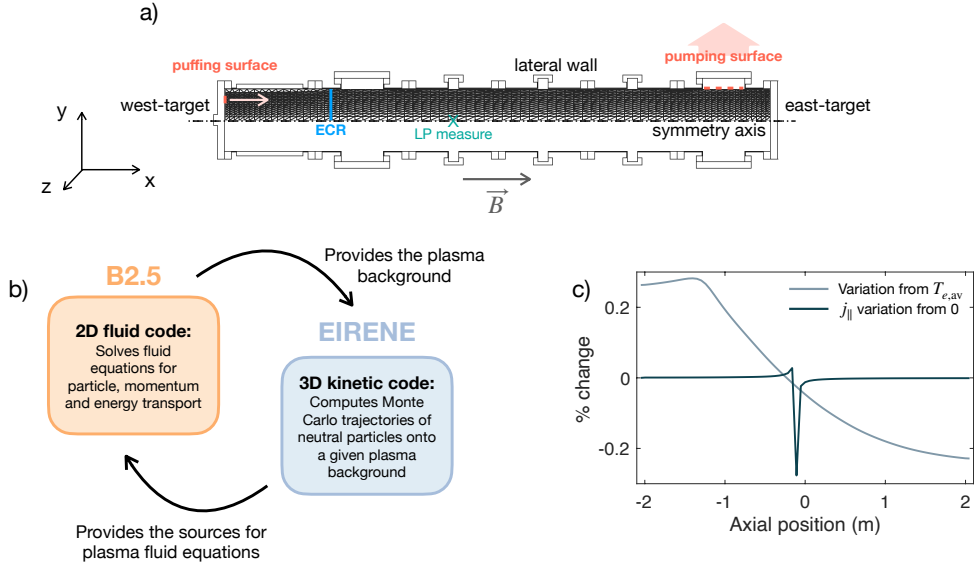


Figure 2. a) 2D mesh used for the SOLPS-ITER simulations. The neutral gas is fed in through a nozzle located on the west-target and it is removed by two turbomolecular pumps, modelled by two partially absorbing surfaces (red dashed lines). ECR position is shown in blue. b) Block diagram of the two main modules of the SOLPS-ITER code and the basic coupling strategy. c) Percentage change of the axial electron temperature and the axial current density j_x , obtained from a SOLPS-ITER simulation with $P_{ext} = 540\text{W}$ and 20sccm gas seeding.

ion energy balance equations should be considered when conduction-limited or detached regimes are of interest.

The normalized form of the equations is reported, for the sake of completeness, in [Appendix A](#).

3. 2D simulations of helium plasma with SOLPS-ITER

The SOLPS-ITER code is one of the most advanced numerical tools for edge plasma simulation in tokamaks. As shown in figure 2.b, the code is based on the coupling of two main modules: a two-dimensional plasma fluid solver, B2.5, and a 3D Monte Carlo code for neutral transport, EIRENE. Although the code was developed for the modelling of plasma boundary in tokamaks, its application to the cylindrical geometry of a LPD is found in few works, e.g. [49, 50], and a systematic analysis of SOLPS-ITER equations in linear geometry is reported in [26].

In this section, we present original simulations of a pure helium plasma in the linear

device GyM: 25 simulations were performed varying the total external power absorbed by the electron population ($P_{\text{ext}} = 180 \text{ W}, 360 \text{ W}, 540 \text{ W}, 720 \text{ W}, 900 \text{ W}$) and the neutral puffing intensity ($\text{Gas}_{\text{in}} = 5 \text{ sccm}, 10 \text{ sccm}, 15 \text{ sccm}, 20 \text{ sccm}, 25 \text{ sccm}$). Before analysing the results of these simulations and comparing them with the point model, in this section we discuss the simulation set-up and we use SOLPS-ITER results to discuss the hypothesis of the point model.

As discussed in [26], the SOLPS-ITER fluid model can be imply to satisfactory describe even low collisional plasmas, as those of GyM. Kinetic corrections to the fluid approach are taken into account in the code using the strategy of flux limiter [15]. This scheme avoids unphysically large values for the transport coefficients, owed to large particle collision times, imposing an artificial, but physically consistent, limit to the corresponding fluxes.

The two-dimensional mesh used in this study is shown in figure 2.a. Perfect axial symmetry was assumed. Simulations were performed employing the physical model described in [26]: no drift velocities were considered and currents only developed in the direction parallel to \vec{B} .

The boundary conditions imposed are the standard SOLPS-ITER ones [12]: sheath boundary conditions at the east and west targets and exponentially decaying density, temperature and potential profiles at the lateral wall boundary, with decay lengths $\lambda_n = 5 \text{ cm}$, $\lambda_T = 5 \text{ cm}$ and $\lambda_\phi = 10 \text{ cm}$, respectively. At the boundary corresponding to the symmetry axis, zero particle and heat fluxes are imposed.

The external power density profile associated to the 2.45 GHz microwave source is modelled with a gaussian axial profile, peaked at the position of the electron cyclotron resonance (ECR) (see figure 2.a), and it is constant along the radial coordinate. Anomalous particle and heat transport is treated in the diffusion approximation, with anomalous diffusion coefficients $D_\perp = 0.5 \text{ m}^2/\text{s}$ and $\chi_\perp = 1.5 \text{ m}^2/\text{s}$, respectively. These values of anomalous transport coefficients are consistent with the ones chosen in previous simulations of GyM with SOLPS-ITER [26].

Neutral particles are fed in through a puffing surface, located at the west target and removed through a pumping surface, with albedo $p_a = 0.018$. The reactions with neutrals considered in EIRENE are electron impact ionization and recombination. Among the default set of reactions for helium plasmas, we did not consider neutral-neutral elastic collisions. Ion-neutral elastic collisions, on the other hand, are not included in the default reaction set, hence we neglected them. The latter assumption implies that ion-neutral friction is not included in our SOLPS-ITER simulations, as it will be further discussed in section 4.2. Finally, concerning the modelling of radiative electron heat losses (EHL), only electron collisions resulting in ion excitation are considered, while the energy lost in the excitation of neutral atoms is not considered. This will be discussed in details in section 4.1.

The first hypothesis of the global model to be verified is the constancy of the ion temperature, equal to room temperature (0.025 eV). According to the simulations performed with SOLPS-ITER, the volume average ion temperature is found to be in the range $T_i \sim 0.1-0.2$ eV for all the simulations performed. In particular, it slightly increases with the power absorbed by electrons and it slightly decreases increasing the background neutral pressure. Although the values found by SOLPS are higher than the ambient temperature, the neglect of T_i and its variation may be considered a good approximation since the hypothesis $T_e \gg T_i$ is well verified ($T_e \sim 5 - 10$ eV in our system). Moreover, as will be shown in section 4.2, the value of T_i has little influence on the results obtained with the point model.

The second hypothesis was about the possibility to compute electron energy sink at the targets through a simplified sheath transmission approach. To do so, we assumed parallel ambipolarity, $j_x = 0$, and we neglected conduction heat fluxes, i.e. the temperature gradients in the direction along \vec{B} . In figure 2.c, the axial profile of the percentage of variation of the electron temperature and the parallel current density is shown. The temperature variation along x is computed as the difference of the axial average $T_{e,av}$ and local $T_e(x)$ electron temperature, normalized to the average one, $1 - T_e(x)/T_{e,av}$. The parallel current density is evaluated through the difference of the axial electron and ion velocities, normalized to the ion one, $1 - v_{x,e}(x)/v_{x,i}(x)$. Both these quantities are, as supposed, negligible being below 1%. Data shown in figure 2.c are taken from the SOLPS-ITER simulation at $P_{ext} = 540$ W and $Gas_{in} = 20$ sccm and they are representative of the results of all the 25 simulations performed.

According to SOLPS-ITER simulations, moreover, the parallel electron heat flux is much larger than the radial one, $q_x \gg q_y$, justifying the neglect of radial heat fluxes in the 0D model.

Finally, the multi-fluid simulations confirms that only singly ionized species ($Z = 1$) are relevant in the conditions under analysis in this work.

4. Results and discussion

4.1. Comparison and interpretation of SOLPS-ITER results through the point model

We start the results discussion, analyzing the outcomes from SOLPS-ITER simulations. To have a direct comparison with the results of the point model, we will consider volume averages of the two-dimensional results of the code. These quantities are computed by SOLPS-ITER as the volume integral of the variable divided by the volume occupied by the plasma, e.g. for plasma density $\int_{Vol_i} n_i dV / \int_{Vol_i} dV$.

In figure 3.a), the volume average of the two-dimensional plasma density and electron temperature is shown. The left column shows the results of the 25 simulations described in section 3, plotted as a function of the neutral puffing strength. The results of the

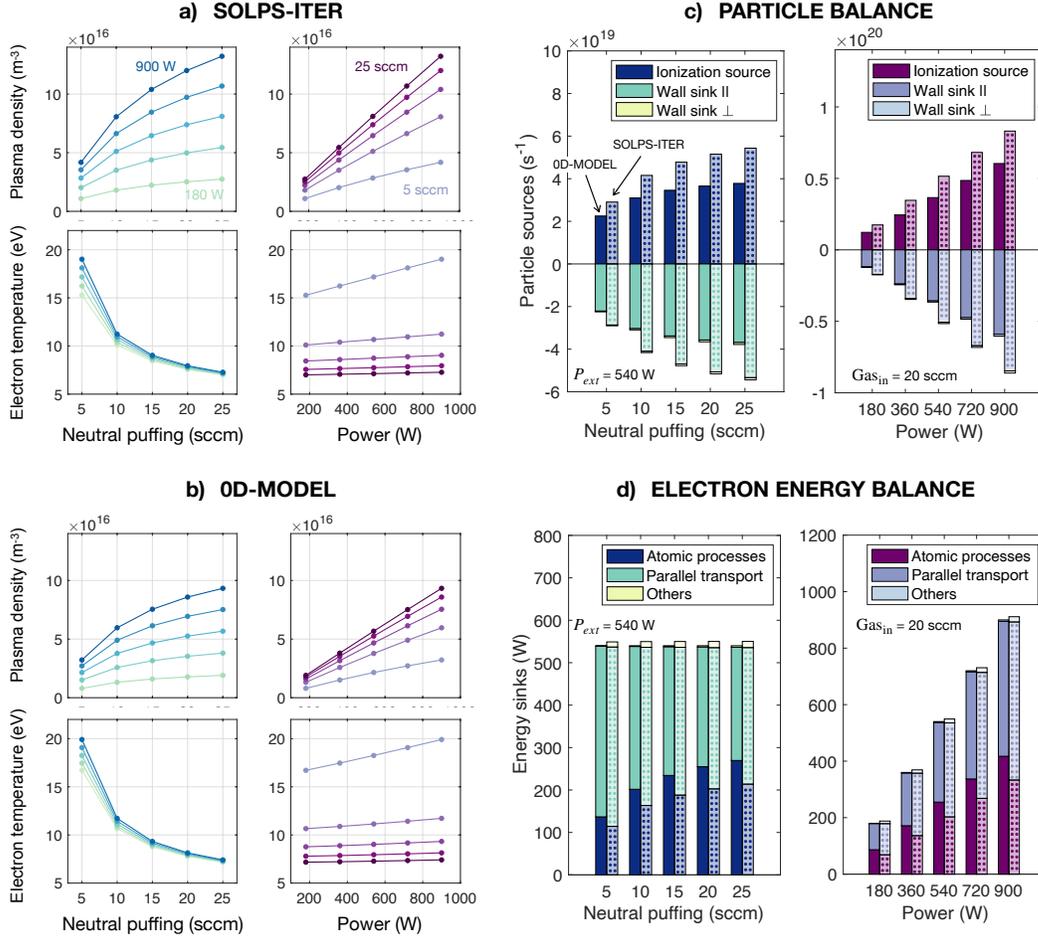


Figure 3. **a)** Results of SOLPS-ITER simulations, volume averaged. **b)** The same quantities are computed using the point model. **c)** Comparison of the particle balance terms computed by the point model (filled) and by SOLPS-ITER (dotted pattern). **d)** Comparison of the electron energy balance contributions computed by the point model (filled) and by SOLPS-ITER (dotted pattern).

simulations are shown with markers and their interpolation intends to improve the readability of the graphs. Different curves correspond to different values of external input power, according to the colorbar below the graphs. The right column shows the same results, plotted as a function of the external power and different lines correspond to different puffing strengths.

From a first qualitative analysis of the results, we can see that the plasma density increases both with the puffing strength and with the external power, but two different functional dependencies are observed: it is almost linear with the power $n_i \sim P_{ext}$, while, in first approximation, for the puffing intensity we can guess $n_i \sim (\text{Gas}_{in})^a$, with $a < 1$. The electron temperature decreases with the puffing strength and increases almost linearly with the external power. The slope of $T_e(P_{ext})$ is higher at low puffing intensities,

while it tends to flatten for higher neutral pressures.

In figure 3.b), results from the steady-state solution of the point model are reported. The same 25 combinations of external power and puffing strength used in the SOLPS-ITER simulations were analyzed. In the point model, the parallel effective transport coefficient was set to $\alpha = 1/2$, implying no ion-neutral friction. The radial diffusion coefficient and the density decay length were set to $D_{\perp} = 0.5 \text{ m}^2/\text{s}$ and $\lambda_n = 5 \text{ cm}$ respectively, as in the SOLPS simulations. Finally, the pumping speed is computed as $S_P = A \times p_a \times 3.638 \times \sqrt{T_n/m_n}$, where A is the effective exposed area of the pumps and p_a is the absorption probability of the pumping surfaces, according to EIRENE user manual (<http://www.eirene.de>). Assuming $p_a = 0.018$, the resulting speed was $S_P = 760 \text{ ls}^{-1}$.

Comparing figure 3.a and figure 3.b, we observe a good qualitative agreement of the results from the two models. The point model is able to reproduce the general trends of n_i and T_e obtained with SOLPS, both as a function of P_{ext} and Gas_{in} .

To better investigate the reliability of our point model, we also compared the individual source and sink terms of the particles and energy balance equations computed by the two models. Results of this comparison are shown in figure 3.c, for particle balance, and 3.d), for internal energy balance[§]. For each value on the abscissa, we compare the filled bar, obtained from the point model, with the dotted pattern bar, which corresponds to sources/sinks computed by SOLPS-ITER.

There is an exact correspondence between the contributions to particle balance in our model and in SOLPS-ITER, by construction. On the other hand, few comments are needed concerning the electron energy balance. The SOLPS-ITER *Parallel transport* term is computed as the sum of the fluxes at the targets and the convective heat loss, associated with $\partial u_e/\partial x$. In our model, this corresponds to the electron heat losses at the sheath entrance. In *Others*, our model only contains electron thermal equilibration, while the contribution from SOLPS-ITER simulations also includes, radial heat losses and heat conduction contributions. In the bar plots, the trends of the different contributions as a function of P_{ext} and Gas_{in} are shown for a fixed value of the other variable.

From the results shown in figures 3.c and 3.d, we can conclude that our model includes all the relevant particles and energy sources and sinks that are implemented in SOLPS-ITER and, moreover, it successfully captures their qualitative trends as a function of P_{ext} and Gas_{in} .

Comparing figure 3.a and figure 3.b from the quantitative point of view, however, some differences are observed in the values of n_e and T_e . To measure the discrepancy between the two models, we assessed the maximum relative difference of the results for each value of P_{ext} and Gas_{in} . This quantity is computed as $D_{\%} = (R_{PM} -$

[§] The energy balance in figure 3.d only contains internal energy dissipation mechanisms, so that the sum of all the contributions is equal to the externally supplied energy.

$R_{SOLPS})/\min(R_{PM}, R_{SOLPS})$, where R_{SOLPS} and R_{PM} are the average results from SOLPS and the steady-state solution of the point model, respectively. $D\%$ is plotted in figure 4 as a function of Gas_{in} (green lines).

The biggest difference is in the plasma density: the point model underestimates n_i about $\sim 30\%$ to $\sim 40\%$ with respect to SOLPS. The discrepancies in both the electron temperature and neutral density are limited, around 10% or below.

The cause for different n_i outcomes is found in the different modelling of the atomic excitation process. As discussed in section 3, SOLPS neglects neutral excitation and the corresponding EHL. From the post-processing of SOLPS simulations, we observed that a negligible fraction of the input power (below 1%) is lost by electrons through excitation processes. The 0D model, on the contrary, includes radiative contribution from neutral excitation and predicts that $\sim 20\%$ of input power is radiated following neutral de-excitation (see section 4.2).

To reduce the differences between the two models, we turned off radiative heat losses also in the point model, setting $R_{i,n,\text{rad}} = 0$ in equation (3). We performed again the 25 simulations, varying P_{ext} and Gas_{in} , and we compared the outcomes in terms of percentage difference. From figure 4, we observed that, neglecting radiative EHL, $D\%$ for n_i is more than halved in magnitude, with respect to the case with the radiative losses. $D\%$ for electron temperature and neutral density, instead, is almost unchanged. To summarize, if we adopt SOLPS-ITER physical model for radiative losses, i.e. we neglect contributions from neutral excitation in the point model, we obtain a very satisfactory agreement. The maximum relative difference in the simulation results is always between $\sim 10\%$ and $\sim 20\%$, in the range of parameters considered.

Another relevant aspect about the importance of excitation processes in LPDs needs to be pointed out. According to our previous work [26], SOLPS-ITER simulations of pure Ar plasma predict that a relevant fraction of input power is dissipated through electron excitation processes. Also in this case SOLPS does not include electron-neutral excitation, so that we must assume that the ion excitation is important in this case. This is readily seen, comparing the rate coefficients for the two species. At the temperature of $T_e \sim 7\text{eV}$, $R_{i,\text{rad}} \sim 5R_{n,\text{rad}}$ for argon, while for helium an opposite scaling holds, $R_{n,\text{rad}} \sim 10R_{i,\text{rad}}$. This physical difference between He and Ar, together with the very low degree of ionization of the plasmas we are considering, led us to conclude that in helium most of the radiated power is caused by electron excitation of neutral atoms, while in argon also ion excitation is an efficient dissipative mechanism.

In conclusion, the previous discussion provides a detailed comparison of results from SOLPS-ITER and the point model and it highlights two important aspects: first, the contribution due to the interaction between electron and neutral atoms, in a weakly ionized plasma, is not negligible and has effects on the steady-state plasma; second, the relative contribution of the different atomic processes is strongly dependent on the plasma species that is considered.

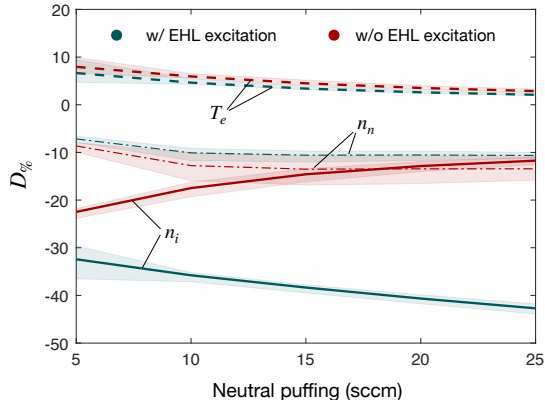


Figure 4. Percentage difference of the results from the two models. Lines refer to the average over different external power values and the shadowed region is the maximum variation from the mean, in the range of considered external powers.

Table 2. Summary of the different parametric studies performed with the point model.

#	Difference from Reference	Description
(0)		Reference case ($P_{\text{ext}} = 1 \text{ kW}$ and $\text{Gas}_{\text{in}} = 20 \text{ sccm}$)
(1)	$D_{\perp} = 0$	Radial diffusion turned off
(2)	$R_{i,n,\text{rad}} = 0$	Radiative electron heat loss turned off
(3)	$S_m = -m_i \nu_{in} n_i (v_i - v_n)$	Ion-neutral friction turned on
(4)	$T_i = 0.2 \text{ eV}$	T_i value taken from SOLPS simulations
(5)	$P_{\text{ext}} = 5 \text{ kW}$ and $\text{Gas}_{\text{in}} = 2000 \text{ sccm}$	Typical divertor relevant conditions in a LPD

4.2. Quantitative analysis of the contributions to the plasma balance equations

In this section, we present an analysis of the sensitivity of the point model with respect to different terms in the equations and different physical assumptions. The advantage of performing such analysis with a simple tool like the point model rather than with a code like SOLPS-ITER is twofold: first, an enormous saving in terms of computational resources can be obtained, which in turn could allow to perform parametric studies spanning variables over a wider range of values; second, interpreting the single contribution of each term is much more immediate and transparent due to the simpler equations.

The analysis is performed comparing the results from a reference case, with other 5 point model simulations, in which one parameter is changed at a time. The reference case uses all the common inputs of the simulations described in section 4.1, with an external power $P_{\text{ext}} = 1 \text{ kW}$ and a puffing strength $\text{Gas}_{\text{in}} = 20 \text{ sccm}$. The difference with respect to the reference case for the other five cases are summarized in table 2.

Figure 5.a shows the steady-state T_e , n_i and n_n and figure 5.b the EHL contributions for the six cases under analysis.

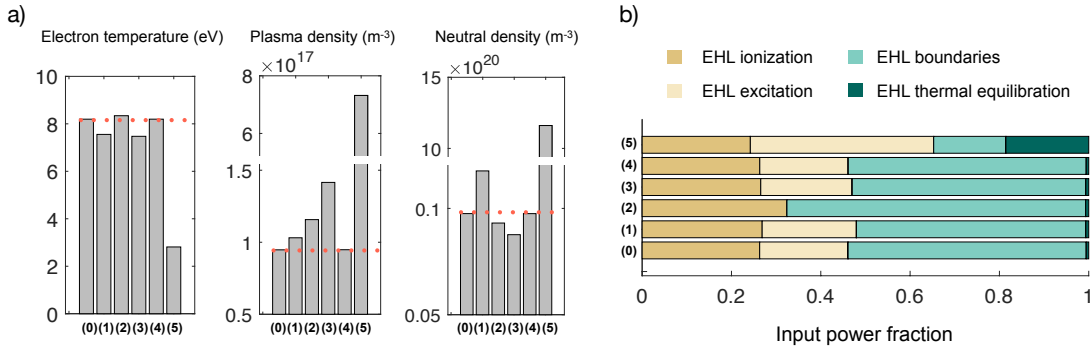


Figure 5. Sensitivity of point model to different parameters. **a)** Steady-state results of electron temperature, plasma and neutral density are shown. The red dotted line represents the values of case (0). **b)** EHL contributions, normalized to the external power. The cases considered are summarized in table 2;

We start making a general comment on the electron energy balance. The electron heat loss contributions of equation (3) are reported in the bar chart of figure 5.b, normalized to the input power. This graph shows in an immediate way the fraction of external power that is dissipated by each of the considered mechanisms: e.g. for the reference case (0) almost half of the external power is dissipated through atomic processes of ionization and neutral excitation and the other half through the sink action of the wall. The thermal equilibration contribution is just few percent of the input power and the electron-ion excitation is negligible.

Effect of radial diffusion: Case (1) investigates the effects of radial diffusion, by setting $D_{\perp} = 0$ in the expression for $\Gamma_{i,\text{wall}}$. From figure 5.a, we observe that the overall effect is a decrease of the electron temperature and an increase of both the plasma and neutral densities. The relative importance of the different EHL mechanisms, shown in figure 5.b, is not greatly affected, although a slightly higher fraction of energy is dissipated through atomic processes rather than at the boundaries.

Figure 6 shows how the plasma and neutral densities and electron temperature are affected by a change in the anomalous diffusion coefficient D_{\perp} in the range $0 - 50 \text{ m}^2\text{s}^{-1}$, also investigating the effect of different input conditions. A trend consistent with the one observed in case (1) is seen. Increasing the value of D_{\perp} produces an increase of T_e and a decrease of both n_i and n_n . Explaining the observed trends, however, is not trivial, due to non-linearity and strong coupling between equations (1), (2) and (3). Moreover, the magnitude of the effect on T_e , n_i and n_n , which results from a variation of D_{\perp} , strongly depends on the overall system conditions, i.e. on the model inputs P_{ext} and Gas_{in} . Due to its relevance in plasma edge modelling, we plan to further explore the effect of D_{\perp} on the system parameters in future studies.

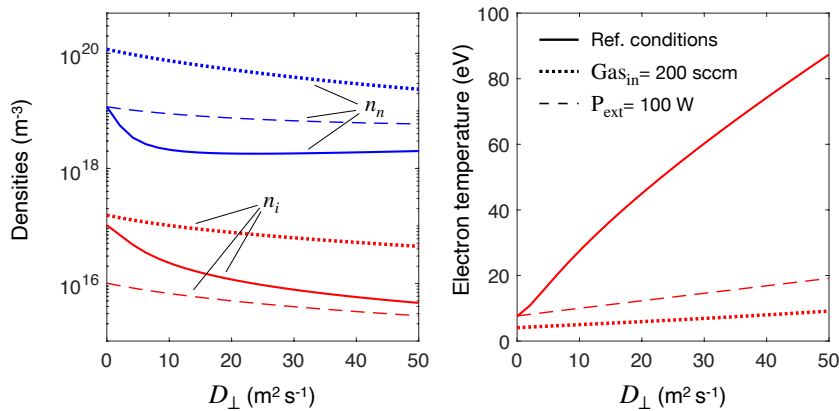


Figure 6. Plasma density (red), neutral density (blue) and electron temperature as a function of the anomalous diffusion coefficient D_{\perp} .

Effect of electron excitation processes: In light of the discussion made at the end of section 4.1, here we further analyze the effect of the electron heat losses related to radiative dissipation, as computed by the point model. In case (2), we study the effect of neglecting this contribution from the electron energy balance, which for an helium plasma is what is done in SOLPS simulations. The main effect is observed on the steady-state value of the plasma density, which is found to be inversely proportional to the values of $R_{i,n,\text{rad}}$. In particular, with $R_{i,n,\text{rad}} = 0$, n_i increases by $\sim 22\%$. Compare case (0) and case (2) in figure 5.a. Observing the energy balance for the two cases, in figure 5.b, we see that almost the same percentage increase ($\sim 23\%$) is observed in the EHL contribution due to ionization. The lack of power dissipation due to electron excitation processes, is compensated by an higher power fraction lost in ionization, which in turn seems to lead to almost the same percentage increase in the plasma density. To test this hypothesis, the opposite trend was studied, enhancing the effect of radiative dissipation by a factor of 5 and keeping all the other parameters constant. A reduction in the plasma density by $\sim 45\%$ was observed, together with a reduction of roughly the same amount in the fraction of power dissipated by ionization.

Effect of ion-neutral friction: In SOLPS, ion-neutral friction is computed only between the main hydrogenic neutral and ion species and, since we are considering here pure helium plasma, it is equal to zero. This contribution is introduced in the point model as discussed in section 2. Comparing case (0) and case (3) in figure 5.a, we observe that once again the main effect is on the plasma density, which is increased by around $\sim 50\%$. However, this time the increase of the plasma density is not due to an increased ionization fraction, but rather to a reduction of the ion sink to the wall. The

effective parallel transport coefficient α is indeed reduced to 0.41. This confining effect is the well known collisional drag due to ion-neutral friction [1].

Effect of ion temperature: In section 3, we saw that the average ion temperature computed by SOLPS is up to one order of magnitude higher than the room temperature. To assess T_i effect on the 0D results, case (4) considers $T_i = 0.2$ eV. Comparing the results of case (4) and case (0), in figure 5, no significant variations are observed. To extend the study, the T_i value was changed over a wide range, from room temperature up to the electron temperature, however no significant variation was observed in the final plasma state. The negligible effect of the ion temperature can be traced back to a low electron-ion collision frequency. This in turn causes a small fraction of the electron energy to be lost by thermal equilibration with ions.

Divertor relevant plasma regime: As a last sensitivity study, case (5) tests the point model in a different plasma regime than the one which characterizes the GyM device. As discussed in section 1, divertor relevant particle fluxes can be obtained in many LPDs. Devices with these features are typically characterized by higher input powers and much higher neutral background pressures than the ones allowable in GyM [32].

Knowing the limits that this point model can have in regimes where conduction and temperature gradients are important, we anyway test it setting the external power to $P_{\text{ext}} = 5$ kW and the puffing intensity to $\text{Gas}_{\text{in}} = 2000$ sccm, in case (5). From figure 5.a, we see that neutral and plasma density are greatly increased with respect to the reference case: n_n increases by 2 orders of magnitude and n_i by a factor ~ 10 . The cause for this increase is related to the 2 order of magnitude increase in the value of $\Gamma_{n,\text{puff}}$.

Coming to the power balance analysis, comparing case (0) to case (5), we observe important changes in the relative weight of the different contributions. Ionization and excitation reactions dissipate more than $\sim 60\%$ of the input power and the EHL due to the thermal equilibration is increased significantly. The cause for both these observations can be traced back to an increase in the frequency of collisions among particles. In light of a comparison with the SOLPS physical model, it is important to note that according to our 0D model, most of power dissipated by thermal equilibration, is due to collisions with neutral particles. SOLPS-ITER neglects this term but, as for neutral excitation, its contribution can be relevant when modelling weakly ionized plasmas in LPDs.

4.3. Analytical formulae

The simple form of equations (1), (2) and (3) is well suited to be approximated with analytical expressions. In this section, we derive expressions for the plasma and neutral density as functions of the electron temperature. We assumed steady-state conditions, neglecting all the temporal derivatives, and perfect momentum conservation, so that the effective transport coefficient in $\Gamma_{i,\text{wall}\parallel}$ is constant, $\alpha = 1/2$.

In computing the rate coefficients for the atomic processes of electron ionization and excitation, only the temperature dependence was considered, thus disregarding the weak effect of the electron density.

With these assumptions, the neutral density n_n is promptly obtained from equation (1):

$$n_n(T_e) = \frac{\Gamma_{i,\text{wall}} + R_{\text{rc}}n_i}{R_{\text{iz}}} \simeq \frac{\Gamma_{i,\text{wall}}}{R_{\text{iz}}} \quad (9)$$

The latter expression is obtained neglecting recombination, since $R_{\text{rc}} \ll R_{\text{iz}}$ except at very low electron temperature typical of detached plasmas, $T_e \lesssim 1$ eV [30].

The electron temperature dependence of the RHS of equation (9) is embedded both in $\Gamma_{i,\text{wall}}$, through the Bohm velocity $u_B \sim \sqrt{T_e}$, and in the ionization rate coefficient R_{iz} . The analytical expression for the plasma density is instead obtained from the electron energy balance. Substituting equation (9) into equation (3), disregarding thermal equilibration and the electron-ion excitation which, as discussed in section 4.1, play a minor role in determining He plasma behavior with respect to the other atomic processes, one gets the following expression:

$$n_i(T_e) = \frac{P_{\text{ext}}}{\text{Vol}_i} \left[\Gamma_{e,\text{wall}}T_e + \left(E_{\text{iz}} + \frac{E_{n,\text{rad}}R_{n,\text{rad}}}{R_{\text{iz}}} \right) \Gamma_{i,\text{wall}} \right]^{-1} \quad (10)$$

The analytical profiles of plasma and neutral density as a function of the electron temperature is shown in figure 7.a with dashed lines. The same input parameters of the reference case of section 4.2 are used.

Observing figure 7.a, one immediately notes the unphysical increase in the neutral density at low temperatures. This is easily explained remembering that, to obtain equation (9), we did not consider important effects on neutral particles, e.g. their removal by turbomolecular pumps. The simplest possibility, adopted in this work, to avoid diverging neutral densities and to keep the equations (9) and (10) as simple as possible is to limit the range of applicability of those equations to a maximum value of n_n equal to $n_{n_\infty} = \Gamma_{n,\text{puff}} / (\Gamma_{n,\text{pump}} \text{Vol}_n)$. This value corresponds to the stationary neutral density set by a given combination of puffing strength and pumping speed, as discussed in more details in section 4.4. The analytical profiles obtained limiting the neutral density to n_{n_∞} are shown in figure 7.a with solid lines, for $\text{Gas}_{\text{in}} = 20$ sccm and dotted lines, for $\text{Gas}_{\text{in}} = 2000$ sccm. As can be seen, increasing the neutral puffing strength increases the upper limit on n_n and allows to apply equations (9) and (10) up to lower T_e . In the limit $n_{n_\infty} \rightarrow \infty$ the full non-limited behavior is recovered.

Exploiting equations (9) and (10), it is possible to obtain a simple analytical expression for the ionization degree of the plasma $\theta_{\text{iz}}(T_e) = n_i(T_e)/(n_i(T_e) + n_n(T_e))$, as

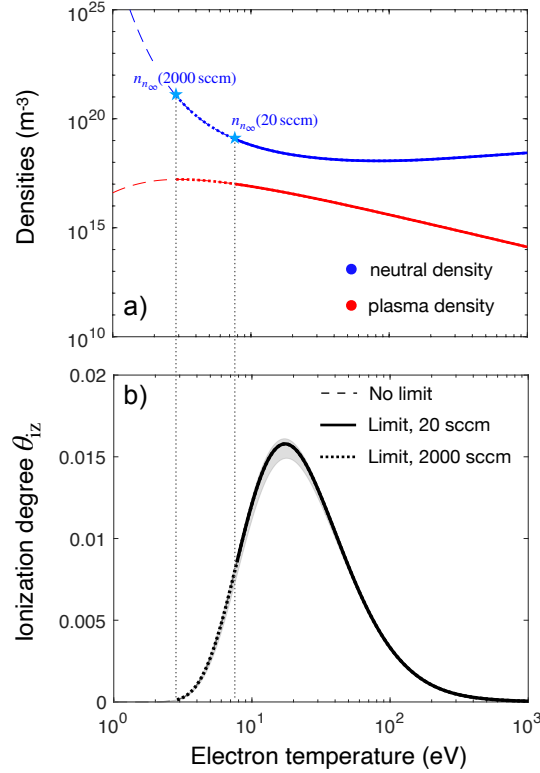


Figure 7. **a)** Analytical profiles for plasma and neutral densities as a function of T_e . **b)** Analytical profiles for the ionization degree θ_{iz} . Dashed lines are obtained without any limiting condition on n_n , while solid and dotted lines refer to profiles obtained limiting $n_n < n_{n,\infty}$, with $\text{Gas}_{\text{in}} = 20 \text{ sccm}$ and $\text{Gas}_{\text{in}} = 2000 \text{ sccm}$, respectively.

a function of electron temperature:

$$\theta_{iz}(T_e) = P_{\text{ext}} \left[\frac{\Gamma_{i,\text{wall}} \text{Vol}_e}{R_{iz}} \left(\Gamma_{e,\text{wall}} T_e + \left(E_{iz} + \frac{E_{n,\text{rad}} R_{n,\text{rad}}}{R_{iz}} \right) \Gamma_{i,\text{wall}} \right) + P_{\text{ext}} \right]^{-1} \quad (11)$$

The profile of $\theta_{iz}(T_e)$ is an asymmetric bell shape, which goes to zero at very low and very high temperatures and has a maximum for T_e around of the ionization energy, $E_{iz} = 24.58 \text{ eV}$ for helium. Considering the reference conditions of section 4.2, the maximum θ_{iz} is below 2%.

Figure 7.b shows the result of plotting equation (11) as a function of T_e . The dashed line, only visible in the left tail of the graph, corresponds to the reference conditions $P_{\text{ext}} = 1 \text{ kW}$ and $\text{Gas}_{\text{in}} = 20 \text{ sccm}$, without limit on n_n ; the solid and the dotted lines are again obtained limiting $n_n \leq n_{n,\infty}$ and correspond to $\text{Gas}_{\text{in}} = 20 \text{ sccm}$ and $\text{Gas}_{\text{in}} = 2000 \text{ sccm}$, respectively. As in figure 7.a, the three curves are superimposed in their region of validity. The shadowed region around the solid line indicates the effect

of changing D_{\perp} in the range $[0 \text{ m}^2/\text{s}, 2 \text{ m}^2/\text{s}]$, showing that varying D_{\perp} in the considered range has little effect on the ionization degree: the latter slightly increases for $0 \text{ m}^2/\text{s} < D_{\perp} < 0.5 \text{ m}^2/\text{s}$ and slightly decreases for $0.5 \text{ m}^2/\text{s} < D_{\perp} < 2 \text{ m}^2/\text{s}$. Finally, although not shown in figure 7.b, we observed that the maximum of $\theta_{\text{iz}}(T_e)$ is directly proportional to the external input power.

As a final analysis of this section, we compared the values of $\theta_{\text{iz}}(T_e)$ computed with the analytical formula in equation (11) to the results of the 0D model and of SOLPS-ITER simulations.

To do so, the 0D model was solved varying the external power in the range $P_{\text{ext}} \in [180 \text{ W}, 10 \text{ kW}]$, the puffing strength in the range $\text{Gas}_{\text{in}} \in [1 \text{ sccm}, 2000 \text{ sccm}]$ and the anomalous diffusion coefficient in the range $D_{\perp} \in [0 \text{ m}^2/\text{s}, 2 \text{ m}^2/\text{s}]$. The ionization degree computed from the results of these simulations are plotted in figure 8.a as scattered points, colored according to the value of P_{ext} . The analytical results are represented with solid lines. They are computed imposing in equation (11) the same P_{ext} values used in the point model, $D_{\perp} = 0.5 \text{ m}^2\text{s}^{-1}$ and $\text{Gas}_{\text{in}} = 2000 \text{ sccm}$. For each value of input power, the simplified analytical expression excellently reproduces the 0D results. The points that deviate from the analytical values are the ones obtained from simulations with $D_{\perp} \neq 0.5 \text{ m}^2\text{s}^{-1}$.

In figure 8.b and 8.c, we compare the analytical and 0D ionization degree with the results from SOLPS-ITER simulations. In figure 8.b, we have shown $\theta_{\text{iz}}(T_e)$, obtained from the 0D model, imposing the five P_{ext} values used in the SOLPS-ITER simulations (see section 3). As discussed before, the maximum of $\theta_{\text{iz}}(T_e)$ is directly proportional to the input power, so that the highest curve in figure 8.b corresponds to $P_{\text{ext}} = 900 \text{ W}$. This curve is compared with the results from SOLPS-ITER simulations at the same input power (red points). With respect to the simulations described in section 3, we performed two additional SOLPS simulations with lower puffing strength, $\text{Gas}_{\text{in}} = 3 - 4 \text{ sccm}$. The seven red points in figure 8.b reproduce the same peaked profile for $\theta_{\text{iz}}(T_e)$ that is obtained both with the analytical formulas and with the point model.

In figure 8.c, we show once again that turning off the EHL contribution due to neutral and ion excitation in the 0D simulations (dashed lines), the agreement between our model and SOLPS-ITER is improved. This effect is more important at high density, as can be seen comparing the results at high ($P_{\text{ext}} = 900 \text{ W}$) and low ($P_{\text{ext}} = 180 \text{ W}$) power.

4.4. Analysis of the time dependent solution with the point model

In all the previous paragraphs, the steady-state solutions of equations (1), (2) and (3) were considered. Here, we investigate the time evolution of these equations towards the steady-state. We considered the input parameters of the reference case, described in section 4.2, and we solved the full ODE system. Solutions as a function of time are

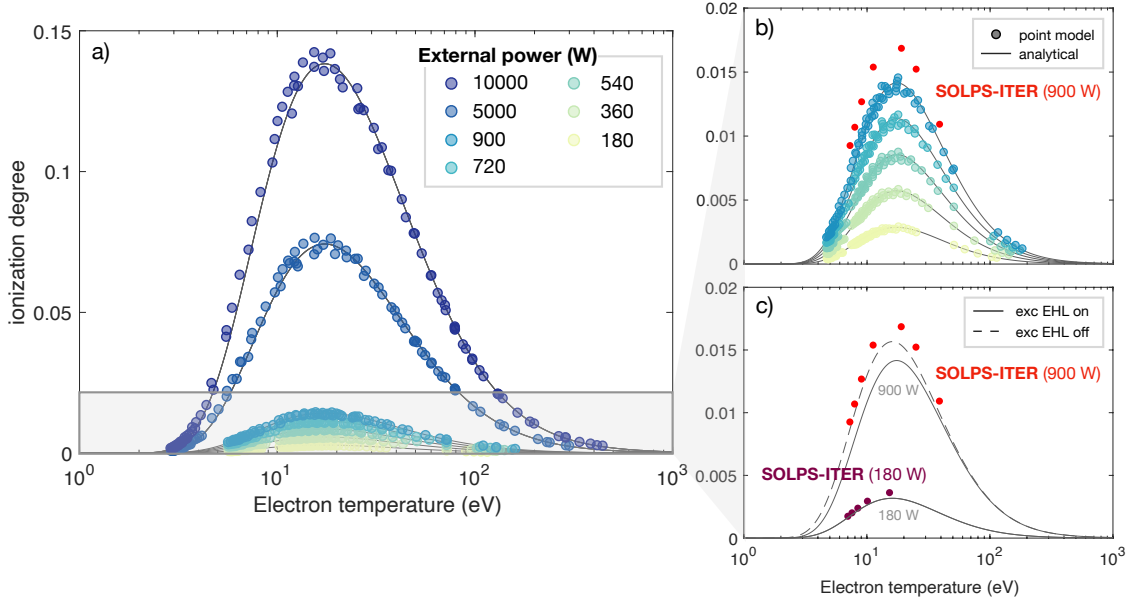


Figure 8. Comparison of θ_{iz} obtained with analytical, 0D and SOLPS-ITER model. **a)** Results of the point model (scatter points) and computed according to the analytical formula in equation (11) (solid lines). **b)** Magnification of the lower region of figure 8.a, corresponding to the power values considered in SOLPS-ITER simulations. The higher values of θ_{iz} correspond to a $P_{\text{ext}} = 900$ W, and it is compared with the results from SOLPS at the same power. **c)** SOLPS-ITER results (points) compared with the analytical expression (11) for θ_{iz} , with (solid) and w/o (dashed) the EHL due to neutral and ion excitation.

plotted in figure 9.

In figures 9.a, 9.b and 9.c, the long-term evolution of the plasma density, electron temperature and neutral density is shown, respectively. The system reaches the steady-state in few fractions of a second and we can roughly estimate the dominant time constant of the system to be $\tau_1 \sim 0.15$ s.

If we compare figure 9.a and 9.b with figure 9.c, we can see that the time evolution of n_n exhibits a quite different behavior with respect to both T_e and n_i . The neutral density transient can be well approximated by simple exponential decay with time constant τ_1 , while the plasma, both in the density and electron temperature evolution, experiences a much faster excursion in the first instants, followed by a small and slow adjustment. The fast transients of plasma density and electron temperature are shown in figures 9.a.1 and 9.b.1, respectively. These transients are characterized by a time constant $\tau_2 \sim 1 \times 10^{-4}$ s.

The physical origin of the slow time constant can be ascribed to the neutral pumping-puffing dynamics, while the very fast transient in plasma density and electron temperature is related to the particle confinement time.

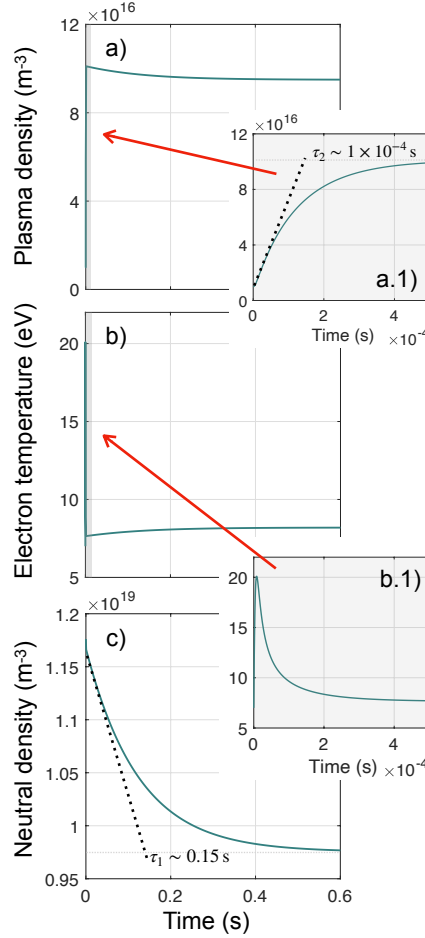


Figure 9. Time evolution of a) plasma density, b) electron temperature and c) neutral density. In the gray boxes the fast time scale $t < 5 \times 10^{-4}$ s is shown for the plasma density and electron temperature in figures a.1) and b.1), respectively.

To see this, we solve the linear ODE that is obtained from equation (2), setting $n_i = T_e = 0$. This equation describes the evolution of the neutral gas in the linear device, when there is no plasma. The analytical solution for the equation is:

$$n_n(t) = n_{n_0} \exp(-t/\tau) + n_{n_\infty} (1 - \exp(-t/\tau)) \quad (12)$$

where n_{n_0} is the initial neutral density value, $n_{n_\infty} = \Gamma_{n,\text{puff}} / (\Gamma_{n,\text{pump}} \text{Vol}_n)$ is the steady-state value of neutral density after the transient and the time constant $\tau = 1/\Gamma_{n,\text{pump}}$ depends only on the pumping speed S_P . With the value used in the 0D model, $S_P = 7601/\text{s}$, we obtain $\tau_{\text{pump}} = 0.13 \text{ s}$, which is indeed of the same order of magnitude of the long-term time constant of the full system.

The ion confinement time due to the sink action of the wall can be estimated as $\tau_{\text{wall}} = \Gamma_{i,\text{wall}}^{-1}$, and for the reference case in section 4.2, using the stationary values for T_e , one gets $\tau_{\text{wall}} = 1.4 \times 10^{-4} \text{ s}$, which again is very close to the time scale of the plasma fast transient, shown in figures 9.a.1 and 9.b.1.

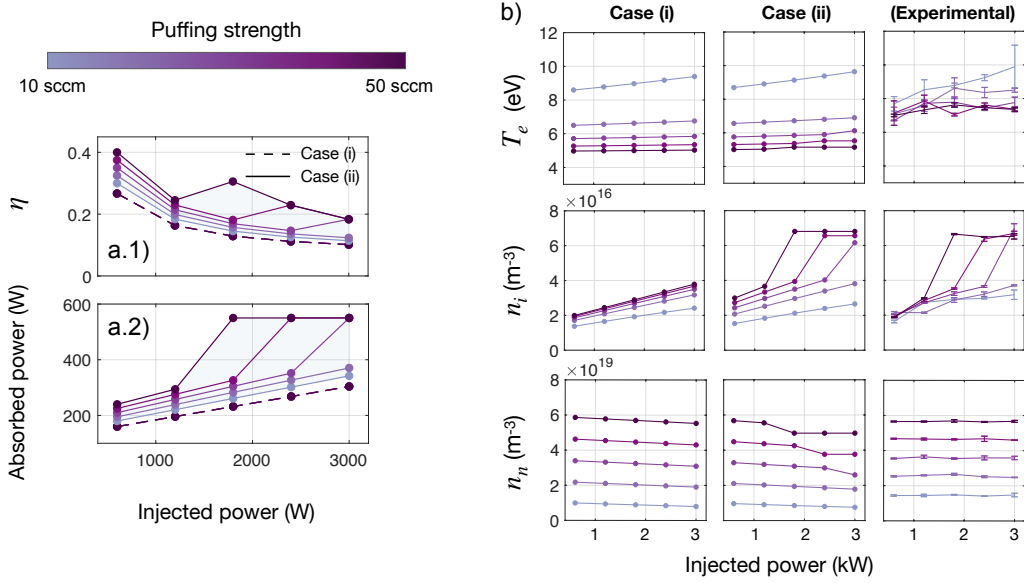


Figure 10. **a.1)** Values of power absorption efficiency η for the simulations of case (i) (dashed) and case (ii) (solid). **a.2)** Absorbed power P_{ext} for the simulations of case (i) (dashed) and case (ii) (solid). **b)** Steady-state T_e , n_i and n_n obtained with the 0D model, case (i) and case (ii), and experimental measures.

The values of τ_{pump} and τ_{wall} , computed with the simple formulae above, slightly differ numerically from the time constants of the full system, due to the non-linearity of equations (1), (2) and (3). Nevertheless, we can recognize a general trend in the system time evolution. Plasma density, electron temperature and neutral density evolve according to two different time scales: the faster one is of the order of the plasma-to-wall transport time, τ_{wall} , and mostly affects the excursion in n_i and T_e , while the slower one τ_{pump} dominates the evolution of n_n and it is connected to the neutral pumping speed.

4.5. Comparison with experimental data

To conclude, in this last section we compare the results of the 0D model with the experimental data from helium discharge in GyM.

During the experiments, the turbomolecular pump worked at $S_P = 520 \text{ l s}^{-1}$. The puffing strength was varied from $\text{Gas}_{\text{in}} = 10 \text{ sccm}$ to $\text{Gas}_{\text{in}} = 50 \text{ sccm}$. Estimates of the plasma density and electron temperature on the axis of the cylindrical chamber were taken using a stainless-steel Langmuir probe. The cylindrical electrode had diameter $D = 2 \text{ mm}$ and length $L = 15 \text{ mm}$. The position where the measure was taken is shown in figure 2.a. The gas pressure was measured with a pressure gauge, located in correspondence of the

duct connecting the chamber to the turbomolecular pump.

As already discussed, in GyM the plasma source exploits ECR heating to supply energy to the electron population in the plasma. An ordinary mode at 2.45 GHz is injected into the chamber and the 1st ECR harmonic is at $B = 0.0875$ T. The experimentally controllable parameter of GyM power source is the injected power, while estimating the amount of power effectively absorbed by the plasma is not easy. This lack of information on the power absorbed fraction introduces an additional unknown in the problem: the ratio of the absorbed to the injected power $\eta = P_{\text{ext}}/P_{\text{in}}$. We will consider it as a free parameter in our simulations and its value will be adjusted to match the experimental plasma density.

The other free parameter in our model is the ratio D_{\perp}/λ_n . As for the previous simulations we set $\lambda_n = 5$ cm, while the coefficient for radial diffusion was fixed at $D_{\perp} = 3$ m² s⁻¹. The value of D_{\perp} was chosen to obtain the best possible agreement with the experimental T_e .

Two sets of hypothesis were used, indicated as case (i) and case (ii), which differ in the values of η . In both cases, we set puffing and pumping to the experimental values, the coefficients for anomalous diffusion as discussed above and the power absorption efficiency as follows:

- Case (i): η does not depend on the puffing strength and it decreases with the injected power (dashed line in figure 10.b.1).
- Case (ii): η increases with the puffing strength and decreases with the injected power. In addition, if $n_i > 4 \times 10^{16}$ m⁻³, we imposed an artificial increase in the value of η , such that $P_{\text{ext}} = 550$ W (solid lines in figure 10.b.1).

The values of the absorption efficiency η and of the absorbed power P_{ext} used in the two sets of simulations are reported in figure 10.a.1 and 10.a.2, as a function of the injected power. The 0D results are reported in figure 10.b. In particular, the first two columns show the steady-state values of electron temperature, plasma and neutral density obtained with the global model for cases (i) and (ii), while the third one shows the experimental data. In all cases, data are shown as a function of the injected power. Comparing the 0D results with the experimental data, we can observe that our model is able to reproduce both from the qualitative and quantitative point of view the data from the LP and the pressure measurements.

In particular, according to the results of the global model, T_e increases almost linearly with the injected power and the slope is bigger at lower puffing strengths. This feature is observed also in the experimental data. The values of the electron temperature, however, are underestimated by the global model for high puffing strengths. A possible explanation could be attributed to the model used for the electron population: a perfectly Maxwellian electron distribution function could be too simplified to satisfactorily describe helium plasma in GyM. In future works, it could be interesting to investigate the effect of non-Maxwellian electrons, e.g. introducing a second low

temperature electron population and study its effect on the global system.

In case (i), the plasma density linearly increases with the injected power, which is also seen experimentally for low Gas_{in} plasmas. We can observe that the slope of the curve $n_i(P_{\text{in}})$ depends on the absorption efficiency as a function of P_{in} : η must decrease with P_{in} to obtain a slope similar to the experimental one, while setting η constant with the power, this would result in a much faster growing $n_i(P_{\text{in}})$. This feature seems to indicate that, increasing the injected power a smaller fraction is absorbed by the plasma or, in other words, that the absorbed power weakly depends on the injected power.

With the hypothesis adopted in case (ii), the 0D results reproduce the experimental jump in the plasma density. In the model, this trend is obtained imposing an artificial increase of P_{ext} for ion densities $n_i > 4 \times 10^{16} \text{ m}^{-3}$. This value is around half of the critical plasma density [45] for an electromagnetic wave at 2.45 GHz, $n_c \sim 7.5 \times 10^{16} \text{ m}^{-3}$. To explain the experimental trend of n_i , we can assume that approaching n_c , some resonant mode conversion mechanism may take place, increasing the fraction of power absorbed by the plasma. Again, this could be an interesting aspect to be investigated in future works.

Finally, we observe that neutral density is almost constant with the injected power. In particular, in case (i), the 0D results well reproduce the experimental data, both qualitatively and quantitatively, while in case (ii) minor discrepancies with experiments are observed where the plasma density is higher. However, it is no surprise that an increase in n_i has no influence in the experimental data available for n_n , since the pressure measurements were done far from the region where the plasma is present. In the future, pressure measurements inside the main plasma chamber should be done to investigate experimentally the relation between n_i and n_n .

5. Conclusions

In this work we have developed an original 0D global model to describe weakly ionized helium plasmas in linear devices.

The 0D model, by its nature, provides a very simple and effective tool to describe complex systems, as plasmas in LPDs. In particular, the one presented here is based on ordinary differential equations, derived from the volume average of standard 2D plasma fluid models.

Advanced 2D simulations of the same physical system were also performed using the state of the art SOLPS-ITER code.

Comparisons between the results obtained with the two approaches, i.e. the 0D model and 2D simulations, showed good agreement and highlighted the relevance of some terms in the modelling of LPDs albeit them being usually neglected in the code.

Specifically, our results show that electron excitation processes of neutral atoms provide an efficient electron heat loss mechanism and affect the final plasma density value.

Moreover, for neutral background pressure of the order of few Pa, which is a typical value in divertor relevant LPDs, thermal equilibration due to elastic collisions between electrons and neutrals may also be important. Both these processes are neglected in the physical model presently implemented in the SOLPS-ITER code.

The 0D model was also used to perform sensitivity studies of the effect of different model parameters. It is worth pointing out that such a large sensitivity study would have required significant computational resources if based on SOLPS simulation results rather than on the simplified 0D model.

The investigation of the time evolution of the system with the global model showed the presence of two different characteristic time scales. The longer time scale ($\tau_1 = 0.1$ s) is related to the neutral pumping speed and governs the dynamics of neutrals, whereas the shorter time scale ($\tau_2 = 1.4 \times 10^{-4}$ s) is associated to the plasma confinement time and is responsible for much faster transients in the plasma density and electron temperature. Lastly, comparisons between the 0D model results and experimental data from the GyM machine showed a satisfactory agreement. In light of these comparisons, it reveals the need for more detailed studies on the power absorption mechanism in ECR-based devices.

In conclusion, our results suggest that our model represents a compelling and promising tool which could be further advanced to be used to support the interpretation and design of future experiments in LPDs.

Acknowledgments

The authors want to thank Dr. D. Dellasega, Dr. A. Pazzaglia and M. Sala for the useful and fruitful discussions. This work has been carried out within the framework of the EUROfusion Consortium and has received funding from the Euratom research and training programme 2014-2018 and 2019-2020 under grant agreement No 633053. The views and opinions expressed herein do not necessarily reflect those of the European Commission and of the ITER Organization.

Appendix A. Normalized point equations

In this section, we report the point model equations in normalized form. This form is the one that has been implemented and solved in MATLAB.

The normalization constants are chosen to be the initial values for densities and temperature, n_{i0} , n_{n0} and T_{e0} respectively, and the plasma transit time computed at the initial time $t_0 = L_{tr}/u_B(T_{e0})$. In this context, non-dimensional variables are indicated with a *tilde* and for this specific problem the new unknowns are: $\tilde{n}_i = n_i/n_{i0}$, $\tilde{n}_n = n_n/n_{n0}$, $\tilde{T}_e = T_e/T_{e0}$ and $\tilde{t} = t/t_0$.

Substituting these expressions into equations (1), (2) and (3) and rearranging, the

following equations are obtained:

$$\frac{d\tilde{n}_i}{d\tilde{t}} = R_{iz}n_{n0}t_0\tilde{n}_i\tilde{n}_n - R_{rc}n_{i0}t_0\tilde{n}_i\tilde{n}_i - \left(\alpha\sqrt{\tilde{T}_e} + \frac{2D_{\perp}}{\lambda_n R}t_0\right)\tilde{n}_i \quad (\text{A.1})$$

$$\begin{aligned} \frac{d\tilde{n}_n}{d\tilde{t}} = & -R_{iz}n_{i0}t_0\tilde{n}_i\tilde{n}_n + R_{rc}\frac{n_{i0}^2}{n_{n0}}t_0\tilde{n}_i\tilde{n}_i + \alpha\beta\frac{n_{i0}}{n_{n0}}\sqrt{\tilde{T}_e}\tilde{n}_i \\ & - \frac{S_P}{\text{Vol}_n}t_0\tilde{n}_n + \frac{\text{Gas}_{in}}{\text{Vol}_n}\frac{t_0}{n_{n0}} \end{aligned} \quad (\text{A.2})$$

$$\begin{aligned} \frac{3}{2}\frac{d\tilde{T}_e}{d\tilde{t}} = & \frac{P_{\text{ext}}}{\text{Vol}_e}\frac{t_0}{n_{i0}T_{e0}}\frac{1}{\tilde{n}_i} \\ & - \left[(E_{iz}R_{iz} + E_{n,\text{rad}}R_{n,\text{rad}})\frac{n_{n0}t_0}{T_{e0}} + \frac{3}{2}R_{iz}n_{n0}t_0\tilde{T}_e \right] \tilde{n}_n \\ & - \left[(E_{i,\text{rad}}R_{i,\text{rad}})\frac{n_{i0}t_0}{T_{e0}} - \frac{3}{2}R_{rc}n_{i0}t_0\tilde{T}_e \right] \tilde{n}_i \\ & - \alpha\left(\frac{1}{2} + |eV_s| + |eV_{ps}|\right)\tilde{T}_e\sqrt{\tilde{T}_e} \\ & + \frac{3}{2}\frac{2D_{\perp}}{\lambda_n R}t_0T_e - \frac{3}{2}\frac{2m_e}{m_i}\nu_{ei}t_0\left(\tilde{T}_e - \frac{T_i}{T_{e0}}\right) - \frac{3}{2}\frac{2m_e}{m_n}n_{n0}R_{n,\text{el}}t_0\left(\tilde{T}_e - \frac{T_n}{T_{e0}}\right)\tilde{n}_n \end{aligned} \quad (\text{A.3})$$

Equations (A.1), (A.2) and (A.3) are solved in MATLAB using the *fsolve* function, to obtain the steady-state values for n_i , n_n and T_e , while time dependent solutions are obtained using a forward Euler finite difference solver.

References

- [1] Stangeby P 2000 *The Plasma Boundary of Magnetic Fusion Devices* Series in Plasma Physics and Fluid Dynamics (Taylor & Francis) ISBN 9780750305594
- [2] Braginskii S 1965 *Reviews of Plasma Physics* **1** 205–311
- [3] Braams B J 1996 *Contributions to Plasma Physics* **36** 276–281 URL <https://doi.org/10.1002/ctpp.2150360233>
- [4] Dudson B *et al.* 2009 *Computer Physics Communications* **180** 1467–1480 URL <https://doi.org/10.1016/j.cpc.2009.03.008>
- [5] Ricci P *et al.* 2012 *Plasma Physics and Controlled Fusion* **54** 124047 URL <https://doi.org/10.1088/0741-3335/54/12/124047>
- [6] Tamain P *et al.* 2016 *Journal of Computational Physics* **321** 606–623 URL <https://doi.org/10.1016/j.jcp.2016.05.038>
- [7] Horsten N *et al.* 2020 *Contributions to Plasma Physics* **60** e201900132 URL <https://doi.org/10.1002/ctpp.201900132>
- [8] Hakim A H *et al.* 2020 *Physics of Plasmas* **27** 042304 URL <https://doi.org/10.1063/1.5141157>
- [9] Bufferand H *et al.* 2015 *Nuclear Fusion* **55** 053025 URL <https://doi.org/10.1088/0029-5515/55/5/053025>
- [10] Wiesen S *et al.* 2015 *Journal of Nuclear Materials* **463** 480–484 URL <https://doi.org/10.1016/j.jnucmat.2014.10.012>
- [11] Bonnin X *et al.* 2016 *Plasma and Fusion Research* **11** 1403102–1403102 URL <https://doi.org/10.1585/pfr.11.1403102>

- [12] Rozhansky V *et al.* 2009 *Nuclear Fusion* **49** 025007 URL <https://doi.org/10.1088/0029-5515/49/2/025007>
- [13] Sytova E *et al.* 2020 *Physics of Plasmas* **27** 082507 URL <https://doi.org/10.1063/5.0006607>
- [14] Kukushkin A *et al.* 1997 *Journal of Nuclear Materials* **241-243** 268–272 URL [https://doi.org/10.1016/s0022-3115\(97\)80047-5](https://doi.org/10.1016/s0022-3115(97)80047-5)
- [15] Fundamenski W 2005 *Plasma Physics and Controlled Fusion* **47** R163–R208 URL <https://doi.org/10.1088/0741-3335/47/11/r01>
- [16] Manz P *et al.* 2020 *Physics of Plasmas* **27** 022506 URL <https://doi.org/10.1063/1.5133839>
- [17] Stangeby P and Moulton D 2020 *Nuclear Fusion* **60** 106005 URL <https://doi.org/10.1088/1741-4326/ab9e16>
- [18] Stangeby P C 2018 *Plasma Physics and Controlled Fusion* **60** 044022 URL <https://doi.org/10.1088/1361-6587/aaacf6>
- [19] Kotov V and Reiter D 2009 *Plasma Physics and Controlled Fusion* **51** 115002 URL <https://doi.org/10.1088/0741-3335/51/11/115002>
- [20] Moulton D *et al.* 2017 *Plasma Physics and Controlled Fusion* **59** 065011 URL <https://doi.org/10.1088/1361-6587/aa6b13>
- [21] Nespoli F *et al.* 2019 *Nuclear Materials and Energy* **18** 29–34 URL <https://doi.org/10.1016/j.nme.2018.11.026>
- [22] Hurlbatt A *et al.* 2016 *Plasma Processes and Polymers* **14** 1600138 URL <https://doi.org/10.1002/ppap.201600138>
- [23] Wauters T *et al.* 2011 *Plasma Physics and Controlled Fusion* **53** 125003 URL <https://doi.org/10.1088/0741-3335/53/12/125003>
- [24] Perillo R *et al.* 2018 *Plasma Physics and Controlled Fusion* **60** 105004 URL <https://doi.org/10.1088/1361-6587/aad703>
- [25] Perillo R *et al.* 2019 *Physics of Plasmas* **26** 102502 URL <https://doi.org/10.1063/1.5120180>
- [26] Sala M *et al.* 2020 *Plasma Physics and Controlled Fusion* **62** 055005 URL <https://doi.org/10.1088/1361-6587/ab7c4f>
- [27] Uccello A *et al.* 2020 *Nuclear Materials and Energy* **25** 100808 URL <https://doi.org/10.1016/j.nme.2020.100808>
- [28] Schneider M *et al.* 2019 *Nuclear Fusion* **59** 126014 URL <https://doi.org/10.1088/1741-4326/ab3de0>
- [29] Hollmann E M *et al.* 2013 *Physics of Plasmas* **20** 093303 URL <https://doi.org/10.1063/1.4821610>
- [30] Hayashi Y *et al.* 2016 *Nuclear Fusion* **56** 126006 URL <https://doi.org/10.1088/0029-5515/56/12/126006>
- [31] Ohno N *et al.* 2019 *Nuclear Materials and Energy* **19** 458–462 URL <https://doi.org/10.1016/j.nme.2019.03.010>
- [32] Tanaka H *et al.* 2020 *Plasma Physics and Controlled Fusion* **62** 115021 URL <https://doi.org/10.1088/1361-6587/abb88f>
- [33] Tanaka H *et al.* 2020 *Physics of Plasmas* **27** 102505 URL <https://doi.org/10.1063/5.0015912>
- [34] Baldwin M and Doerner R 2008 *Nuclear Fusion* **48** 035001 URL <https://doi.org/10.1088/0029-5515/48/3/035001>
- [35] Kajita S *et al.* 2009 *Nuclear Fusion* **49** 095005 URL <https://doi.org/10.1088/0029-5515/49/9/095005>
- [36] Sakamoto R *et al.* 2016 *Nuclear Fusion* **57** 016040 URL <https://doi.org/10.1088/1741-4326/57/1/016040>
- [37] Song K *et al.* 2019 *Nuclear Fusion* **59** 096031 URL <https://doi.org/10.1088/1741-4326/ab2e3c>
- [38] Kreter A *et al.* 2015 *Fusion Science and Technology* **68** 8–14 URL <https://doi.org/10.13182/>

- [fst14-906](#)
- [39] Temmerman G D *et al.* 2013 *Fusion Engineering and Design* **88** 483–487 URL <https://doi.org/10.1016/j.fusengdes.2013.05.047>
 - [40] Ohno N *et al.* 2001 *Nuclear Fusion* **41** 1055–1065 URL <https://doi.org/10.1088/0029-5515/41/8/309>
 - [41] Hollmann E M *et al.* 2002 *Physics of Plasmas* **9** 1226–1232 URL <https://doi.org/10.1063/1.1452103>
 - [42] Rapp J *et al.* 2020 *Fusion Engineering and Design* **156** 111586 URL <https://doi.org/10.1016/j.fusengdes.2020.111586>
 - [43] Blackwell B D *et al.* 2012 *Plasma Sources Science and Technology* **21** 055033 URL <https://doi.org/10.1088/0963-0252/21/5/055033>
 - [44] Diem S J *et al.* 2018 *Physics of Plasmas* **25** 072124 URL <https://doi.org/10.1063/1.5033334>
 - [45] Richardson A S 2019 *NRL PLASMA FORMULARY Supported by The Office of Naval Research* (Washington, DC: Naval Research Laboratory) URL <http://wwwppd.nrl.navy.mil/nrlformulary/>
 - [46] Alves L L 2014 *Journal of Physics: Conference Series* **565** 012007 URL www.lxcat.net/IST-Lisbon
 - [47] Haggmark L and Biersack J 1979 *Journal of Nuclear Materials* **85-86** 1031–1035 URL [https://doi.org/10.1016/0022-3115\(79\)90397-0](https://doi.org/10.1016/0022-3115(79)90397-0)
 - [48] Grisolia C *et al.* 1992 *Journal of Nuclear Materials* **196-198** 281–284 URL [https://doi.org/10.1016/s0022-3115\(06\)80046-2](https://doi.org/10.1016/s0022-3115(06)80046-2)
 - [49] Kastelewicz H and Fussmann G 2004 *Contributions to Plasma Physics* **44** 352–360 URL <https://doi.org/10.1002/ctpp.200410053>
 - [50] Baeva M *et al.* 2007 *Journal of Nuclear Materials* **363-365** 330–334 URL <https://doi.org/10.1016/j.jnucmat.2007.01.029>